Phys Chem Minerals (2015) 42:595–608
DOI 10.1007/s00269-015-0747-8

ORIGINAL PAPER

Single-crystal diffraction and Raman spectroscopy of hedenbergite up to 33 GPa

Yi Hu[1,2] · Przemyslaw Dera[2] · Kirill Zhuravlev[3]

Received: 19 January 2015 / Accepted: 29 March 2015 / Published online: 9 April 2015

Abstract Pyroxenes are important minerals in Earth's upper mantle and subducting plate. Here, we report results of high-pressure single-crystal X-ray diffraction and Raman spectroscopy experiments conducted on natural Ca, Fe pyroxene hedenbergite up to ~33 GPa in diamond anvil cell. Unit cell parameters a, b, c, β and V, as well as bond lengths of hedenbergite are reported within the studied pressure range. Cell parameters exhibit continuous decrease on compression. Axial compressibilities of a, b and c are calculated to be 1.7(2), 4.9(5) and 2.13(9) $\times$ 10^{-3} GPa^{-1}, respectively. Bulk modulus and its pressure derivative are determined to be 131(4) GPa and 3.8(3) by fitting third-order Birch–Murnaghan equation of state. Compression mechanism is dominated by polyhedral and bond compression trends typical of clinopyroxenes. In general, shorter bonds show lower compressibility, and SiO_4, the smallest polyhedron, shows the lowest compressibility. Angle and elongation distortions are reported for the three types of polyhedra at high pressure. Thirteen vibrational modes are observed with Raman spectroscopy up to ~33 GPa. All observed mode frequencies increase as pressure increases.

✉ Yi Hu
yihu@hawaii.edu

[1] Department of Geology and Geophysics, School of Ocean and Earth Science and Technology, University of Hawaii at Manoa, 1680 East West Road, POST Bldg, Honolulu, HI 96822, USA

[2] Hawaii Institute of Geophysics and Planetology, School of Ocean and Earth Science and Technology, University of Hawaii at Manoa, 1680 East West Road, POST Bldg, Honolulu, HI 96822, USA

[3] Argonne National Laboratory, Center for Advanced Radiation Sources, University of Chicago, 9700 S. Cass Ave., Bldg. 434, Argonne, IL 60439, USA

Keywords Hedenbergite · Diopside · Pyroxenes · High pressure · Synchrotron single-crystal X-ray diffraction · Mantle · Subduction zone

Introduction

Pyroxenes are important minerals in the deep Earth. In the bulk mantle, according to pyrolitic compositional model, the top upper mantle is composed of ~65 % olivine, ~20 % pyroxene and ~15 % garnet by volume (Ringwood 1975; Ita and Stixrude 1992). As pressure and temperature increase, pyroxenes gradually dissolve into garnet and form majorite garnet at the base of the upper mantle (Ringwood 1967). Pyroxenes are also abundant in subducting slabs. The oceanic lithosphere is composed of basaltic crust (fine-grained basalt and coarse-grained gabbro), harzburgite, lherzolite and light rare earth element (LREE)-depleted pyrolite. There are ~22 and ~35 % pyroxenes in harzburgite and lherzolite, respectively (Ringwood 1982). As the slab subducts into mantle, the top basaltic crustal layer undergoes eclogitic metamorphism during which plagioclase and some of the clinopyroxenes are consumed to produce garnet (Ringwood 1982). However, recent high-pressure studies show that the dissolution of pyroxene into garnet is kinetically suppressed at temperatures below geotherm (<1000 °C); thus, they may be preserved to much higher pressure in the cool subducting slab (Nishi et al. 2008, 2013; Van Mierlo et al. 2013). Recently, anomalous seismic velocity structures have been observed by different seismic methods and are interpreted as metastable olivine wedge in cold subducting slabs (Jiang et al. 2008, 2015; Kaneshima et al. 2007). It is possible that metastable pyroxenes exist in the cold slabs and even in broader ranges than metastable olivine, due to the higher temperatures defining their metastability limits (Bina 2013).

Pyroxenes, with a general formula M2M1(Si, Al)$_2$O$_6$, belong to the inosilicate family, with crystal structures consisting of alternating layers of tetrahedral chains and layers of octahedrally coordinated cations. The ability of the tetrahedra along the silicate chains to rotate with respect to one another allows the structure to accommodate cations with different ionic radii and charges, leading to a wide range of possible compositions (Cameron and Papike 1981). Recent single-crystal X-ray diffraction studies on pyroxenes (enstatite, diopside, ferrosilite) reported a number of new high-pressure phases under ambient temperature (Plonka et al. 2012; Zhang et al. 2012; Dera et al. 2013a, b; Finkelstein et al. 2014). Hedenbergite is an important Ca, Fe end-member of clinopyroxenes family, and constraining its behavior and physical properties can be useful for modeling the behavior of clinopyroxene solid solutions. Hedenbergite can be found in chondrites (Krot et al. 2000) and skarn, a calcium-bearing rock (Meinert 1992). Hedenbergite has been the subject of several high-pressure studies. Its structure was determined up to ~10 GPa by single-crystal diffraction, and no discontinuous behavior was observed (Zhang et al. 1997). On the other hand, high-pressure nuclear forward scattering (synchrotron Mössbauer) studies up to 68 GPa reported discontinuities at 53 and 68 GPa (Zhang et al. 1999). High temperature and high-pressure phase transformation of hedenbergite were studied up to 40 GPa and ~1200 °C, and decomposition to multiple phases was also observed (Kim et al. 1989, 1991).

Single-crystal diffraction is a powerful tool for resolving variations in the crystal structure. The bond length changes inside the crystal can be useful for predicting crystal behavior at high pressure and calculating element partitioning, as well as thermodynamic properties (Wood and Blundy 1997; Chermak and Rimstidt 1989; Van Hinsberg et al. 2005a, b). Here, we determined the compressibility, structure and vibrational properties of natural hedenbergite by synchrotron single-crystal X-ray diffraction and Raman spectroscopy up to ~33 GPa in diamond anvil cell. Compressibilities and pressure evolution of bond lengths and polyhedral distortion are determined and discussed.

Experimental details

In this study, we used a sample of natural hedenbergite from the University of Arizona RRUFF collection #R070236, with composition $Ca_{1.00}(Fe_{.67}Mn_{.16}Mg_{.17})Si_2O_6$, determined by means of electron microprobe analysis. The ambient unit cell parameters, determined by single-crystal X-ray diffraction at the University of Arizona, are $a = 9.834(6)$ Å, $b = 9.023(5)$ Å, $c = 5.237(2)$ Å, $\beta = 104.70(3)°$ and $V_0 = 449.5(6)$ Å^3. For comparison, the sample used by Zhang et al. (1997) was a synthetic $CaFeSi_2O_6$ hedenbergite.

Table 1 Refinement results of hedenbergite up to 29.9(1) GPa

Pressure (GPa)	1.9(1)	5.9(1)	12.7(1)	18.0(1)	24.5(1)	29.9(1)
Wavelength (Å)	0.3033					
θ range for data collection	1.34–17.39	1.35–13.70	1.37–16.84	1.38–14.97	1.40–17.03	1.41–16.86
No. of reflections collected	480	326	296	329	423	336
No. of independent reflections	206	145	148	157	178	146
No. of parameters refined	35	34	34	34	34	34
Limiting indices	$-14 \le h \le 14$, $-12 \le k \le 10$, $-6 \le l \le 6$	$-13 \le h \le 10$, $-10 \le k \le 8$, $-5 \le l \le 6$	$-11 \le h \le 14$, $-11 \le k \le 6$, $-5 \le l \le 6$	$-11 \le h \le 12$, $-10 \le k \le 7$, $-5 \le l \le 5$	$-14 \le h \le 14$, $-10 \le k \le 10$, $-5 \le l \le 5$	$-13 \le h \le 14$, $-10 \le k \le 8$, $-5 \le l \le 5$
R_{int}	0.0857	0.1301	0.134	0.103	0.0767	0.1005
Final R_1 and wR_2 (reflections $I > 2\sigma(I)$)	0.0509, 0.1019	0.0663, 0.1320	0.0663, 0.1317	0.0682, 0.1548	0.0587, 0.1232	0.063, 0.1354
Final R_1 and wR_2 (all reflections)	0.0526, 0.1023	0.0674, 0.1334	0.0663, 0.1318	0.0688, 0.1550	0.0590, 0.1243	0.0659, 0.1357
Goodness of fit	1.089	1.193	1.092	1.041	1.177	1.056
$\Delta\rho_{max}$, $\Delta\rho_{min}$ (e Å^{-3})	0.706, −0.869	0.828, −0.902	0.760, −1.051	1.125, −1.192	0.873, −0.942	0.800, −0.578
SOF of Fe	81.90 %					
SOF of Mg	18.10 %					

A large approximately 1 mm^3 specimen of hedenbergite was crushed into smaller pieces in a mortar under methanol. One small platelet-shaped crystal with approximate size 0.025 × 0.025 × 0.005 mm was loaded into a diamond anvil cell (DAC). The sample crystal was oriented with [1 1 0] direction along the DAC axis.

Diamond anvils with 0.250-mm culet size and Re gasket preindented to a thickness of ~0.042 mm were used. We utilized a combination of cubic boron nitride cBN (upstream) and tungsten carbide WC (downstream) backing plates. The angular access to the sample through the WC seat was ±13°; however, two additional rotation ranges, from −30° to −20° and from 20° to 30°, could be accessed thanks to the low X-ray absorption coefficient of the cBN seat. In the remaining two rotation ranges, from −20° to −13° and from 13° to 20°, strong powder diffraction signal caused by the transmitted beam touching the WC seat cone contaminated the diffraction images and this data were not used for further analysis. The gasket hole with initial diameter of ~0.160 mm was filled with Ne pressure medium, using the GSECARS/COMPRES gas loading apparatus (Rivers et al. 2008). Two small ruby spheres were placed in the sample chamber together with the sample crystal for pressure calibration. Pressure was calculated from the shift of the R1 ruby fluorescence line (Mao et al. 1986). The diffraction experiments were carried out at the GSECARS facility at APS, Argonne National Laboratory, in experimental station 13IDD. Monochromatic beam with incident energy of 37 keV was focused by a pair of Kirkpatrick–Baez mirrors to a spot of 0.003 by 0.005 mm. Diffraction images were collected using a MAR165 charge-coupled device (CCD) detector, placed at a sample-to-detector distance of approximately 200 mm. During the exposure, the sample was rotated about the vertical axis of the instrument (ω) in the three accessible rotation ranges, with a typical exposure time of 0.5 s/°. Diffraction images were collected at three different detector positions, differing by a translation of 70 mm perpendicular to the incident beam. The detector geometry parameters at each detector position were

Table 2 Structural parameters of hedenbergite as a function of pressure

Pressure (GPa)	1.9(1)	5.9(1)	12.7(1)	18.0(1)	24.5(1)	29.9(1)
Si						
x	0.2873(2)	0.2874(3)	0.2878(3)	0.2868(4)	0.2868(2)	0.2853(4)
y	0.0937(2)	0.0945(4)	0.0946(5)	0.0969(5)	0.0984(3)	0.0991(4)
z	0.2318(3)	0.2313(5)	0.2326(5)	0.2327(5)	0.2341(4)	0.2356(7)
Ca(2)						
x	0	0	0	0	0	0
y	0.3022(3)	0.3045(5)	0.3069(5)	0.3090(5)	0.3111(4)	0.3121(5)
z	0.25	0.25	0.25	0.25	0.25	0.25
Fe(1)						
x	0	0	0	0	0	0
y	0.9078(2)	0.9090(4)	0.9108(4)	0.9102(4)	0.9110(3)	0.9104(4)
z	0.25	0.25	0.25	0.25	0.25	0.25
Mg(1)						
x	0	0	0	0	0	0
y	0.9078(2)	0.9090(4)	0.9108(4)	0.9102(4)	0.9110(3)	0.9104(4)
z	0.25	0.25	0.25	0.25	0.25	0.25
O(1)						
x	0.1185(6)	0.119(1)	0.120(1)	0.119(1)	0.1182(6)	0.118(1)
y	0.0899(7)	0.092(1)	0.095(1)	0.095(1)	0.0944(8)	0.093(1)
z	0.1503(8)	0.152(2)	0.156(2)	0.154(2)	0.150(1)	0.151(2)
O(2)						
x	0.3620(5)	0.3612(9)	0.3598(9)	0.357(1)	0.3548(6)	0.352(1)
y	0.2473(6)	0.249(1)	0.256(1)	0.258(1)	0.2624(9)	0.267(1)
z	0.3248(8)	0.328(1)	0.331(1)	0.333(1)	0.337(1)	0.343(2)
O(3)						
x	0.3511(5)	0.3526(8)	0.3549(8)	0.3563(9)	0.3565(6)	0.3552(8)
y	0.0209(7)	0.023(1)	0.024(1)	0.028(1)	0.0272(8)	0.029(1)
z	0.9916(7)	0.986(1)	0.978(2)	0.987(1)	0.989(1)	0.9878(2)

calibrated with a CeO_2 NIST diffraction standard. In addition to the full-rotation exposures, a step scan with 1° rotation steps was performed at each pressure. The sample was compressed in approximately 5 GPa steps, with full data collection at each step. The pressure range covered was 0.0001–29.9(1) GPa.

Diffraction images were analyzed using the GSE_ADA/RSV software package (Dera et al. 2013a, b). Integrated peak intensities were corrected for Lorenz, polarization, DAC absorption and sample displacement effects using the methods implemented in GSE_ADA (Dera et al. 2013a, b). Because of high incident energy, negligible sample thickness and low X-ray absorption coefficient of the sample at 37 keV, the sample absorption effect was ignored. Corrected peak intensities were used for least-squares structure refinement with SHELXL (Sheldrick 2008), which started from the *C2/c* ambient pressure structure model of Cameron et al. (1973). Because of the limited number of unique observations, anisotropic atomic displacement parameters (ADPs) were used only for the non-oxygen atoms, whereas oxygen atoms were modeled with isotropic ADPs. According to the microprobe analysis, the M2 site was fully (within experimental uncertainty) occupied by Ca^{2+} and any attempts at refining the site occupancy factor (SOF) for this site resulted in convergence to SOF = 1; therefore, in the final refinement, this parameter was fixed to one. Occupancy model was also not refined for Si^{4+} and oxygen sites. For the M1 site, we assumed that Mn^{2+} and Fe^{2+}, having almost the same atomic number, are undistinguishable with X-rays and treated both of these cations as Fe^{2+}. We modeled cation disorder at the M1 site assuming substitution of Fe^{2+}/Mn^{2+} with Mg^{2+} and constraining the sum of the two SOFs to one (no vacancy model). The SOF model of M1 site was only refined at the lowest pressure point and was fixed to be a constant at high pressures. The positions and ADPs of Fe^{2+} and Mg^{2+} were fixed to be the same. The substitution

Table 3 Atomic displacement parameters (Å^2) of hedenbergite as a function of pressure

Pressure (GPa)	U_{11}	U_{22}	U_{33}	U_{23}	U_{13}	U_{12}
1.9(1)						
Si	0.005(2)	0.006(2)	0.010(1)	0.000(1)	0.000(1)	0.000(1)
Ca(2)	0.009(2)	0.011(2)	0.013(1)	0	−0.001(1)	0
Fe(1)	0.005(1)	0.008(2)	0.011(1)	0	0.000(1)	0
Mg(1)	0.005(1)	0.008(2)	0.011(1)	0	0.000(1)	0
5.9(1)						
Si	0.013(3)	0.001(4)	0.011(2)	0.000(1)	−0.001(1)	−0.002(1)
Ca(2)	0.017(3)	0.007(4)	0.013(2)	0	0.001(1)	0
Fe(1)	0.009(3)	0.009(3)	0.012(2)	0	−0.001(1)	0
Mg(1)	0.009(3)	0.009(3)	0.012(2)	0	−0.001(1)	0
12.7(1)						
Si	0.003(3)	0.009(4)	0.008(2)	0.001(1)	−0.002(1)	0.000(1)
Ca(2)	0.018(3)	0.000(4)	0.009(2)	0	0.004(1)	0
Fe(1)	0.002(2)	0.005(3)	0.007(1)	0	0.001(1)	0
Mg(1)	0.002(2)	0.005(3)	0.007(1)	0	0.001(1)	0
18.0(1)						
Si	0.009(3)	0.002(4)	0.008(2)	0.000(1)	−0.001(1)	−0.001(1)
Ca(2)	0.012(3)	0.004(4)	0.012(2)	0	0.001(1)	0
Fe(1)	0.005(2)	0.006(3)	0.011(2)	0	0.000(1)	0
Mg(1)	0.005(2)	0.006(3)	0.011(2)	0	0.000(1)	0
24.5(1)						
Si	0.006(2)	0.005(3)	0.012(2)	0.001(1)	0.000(1)	0.001(1)
Ca(2)	0.008(2)	0.011(3)	0.012(2)	0	0.000(1)	0
Fe(1)	0.006(2)	0.010(3)	0.011(1)	0	0.001(1)	0
Mg(1)	0.006(2)	0.010(3)	0.011(1)	0	0.001(1)	0
29.9(1)						
Si	0.004(2)	0.016(4)	0.008(2)	−0.001(1)	−0.001(1)	−0.001(1)
Ca(2)	0.009(3)	0.008(4)	0.014(2)	0	0.000(1)	0
Fe(1)	0.005(2)	0.013(3)	0.012(2)	0	0.002(1)	0
Mg(1)	0.005(2)	0.013(3)	0.012(2)	0	0.002(1)	0

Table 4 Unit cell parameters of hedenbergite

P (GPa)	a (Å)	b (Å)	c (Å)	β (°)	V (Å^3)	ρ (g/cm^3)
0.00[a]	9.834(6)	9.023(5)	5.237(2)	104.70(3)	449.5(6)	3.586(5)
1.9(1)	9.787(4)	8.953(5)	5.226(1)	104.64(2)	443.1(3)	3.638(2)
5.9(1)	9.706(3)	8.852(4)	5.176(1)	104.29(2)	430.9(2)	3.741(2)
12.7(1)	9.615(4)	8.665(6)	5.111(2)	103.96(3)	413.2(3)	3.901(3)
18.0(1)	9.515(5)	8.591(5)	5.069(2)	103.78(3)	402.4(3)	4.006(3)
24.5(1)	9.480(5)	8.392(6)	5.035(2)	103.63(3)	389.2(3)	4.141(3)
29.9(1)	9.442(5)	8.288(6)	4.997(2)	103.39(3)	380.4(4)	4.237(4)

Standard deviations in the last decimal digit are given in parentheses

[a] Data from RRUFF R070236

model for the M1 site at 1.9(1) GPa, based on refined SOFs for Mg^{2+} and Fe^{2+}/Mn^{2+}, is consistent with the microprobe results. Extinction parameter was also refined. Details of the crystal structure refinements, final fractional atomic coordinates and ADPs, as well as selected bond lengths and angles at the six pressures studied, are presented in Tables 1, 2 and 3. VESTA was used to calculate polyhedral volume.

Raman spectra were collected at GSECARS offline system at the Advanced Phonon Source, Argonne National Laboratory. Raman scattering was excited with 514 nm green laser. The laser was focused on the sample by a 10× objective to a spot of few micrometers. Raman spectra were collected with a Horiba HR460 spectrometer equipped with 1800 lines/mm grating. A 30-μm spatial filter was used. The Roper Scientific LN/CCD-1340/100-EB/1 liquid nitrogen cooled CCD was used as detector.

Results

Axial compressibilities of hedenbergite

Unit cell parameters of hedenbergite up to 29.9(1) GPa are listed in Table 4. Normalized unit cell parameters of this study along with Zhang et al. (1997) are shown in Fig. 1. Our low-pressure results show good agreement with the previous study. No discontinuity in the pressure dependence of any of the parameters is found up to 29.9(1) GPa.

Axial compressibility β_{l0} is defined as

$$\beta_{l0} = \frac{1}{3K_{l0}} = -\left(\frac{1}{l}\frac{\partial l}{\partial P}\right)_T \quad (1)$$

where K_{l0} is the linearized modulus at ambient pressure, l is axis length and P and T represent pressure and temperature, respectively. K_{l0} is obtained by weighted least-squares fit of the second-order linearized Birch–Murnaghan (BM2) equation of state as shown below (Hazen and Downs 2000):

$$P(l) = \frac{3K_{l0}}{2}\left[\left(\frac{l_0}{l}\right)^7 - \left(\frac{l_0}{l}\right)^5\right]. \quad (2)$$

The three crystallographic axes a, b and c of hedenbergite exhibit different compressibilities. The results of linearized second-order Birch–Murnaghan equation of state fitting are shown as solid lines in Fig. 1. Axial compressibility of a, b and c are calculated to be 1.7(2), 4.9(5), 2.13(9) × 10^{-3} GPa^{-1} by BM2. β in Fig. 1 is fit with third-order polynomial fitting.

Equation of state of hedenbergite

The bulk modulus K_{T0} and its pressure derivative K'_{T0} can be determined with a weighted nonlinear least-squares fitting of third-order Birch–Murnaghan equation of state (BM3):

$$P(V) = \frac{3K_{T0}}{2}\left[\left(\frac{V_0}{V}\right)^{7/3} - \left(\frac{V_0}{V}\right)^{5/3}\right]\left\{1 + \frac{3}{4}(K'_{T0} - 4)\left[\left(\frac{V_0}{V}\right)^{2/3} - 1\right]\right\}, \quad (3)$$

where P is pressure and V and V_0 represent the volume at high pressure and ambient pressure, respectively (Hazen

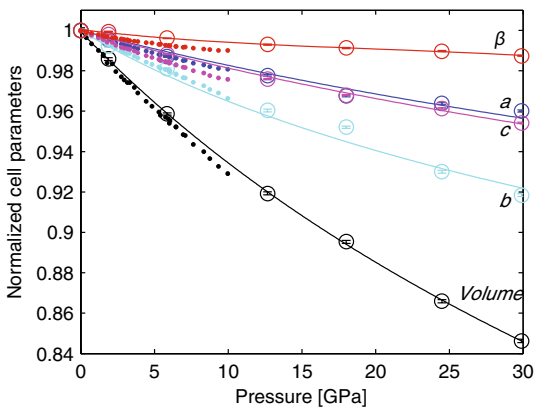

Fig. 1 Pressure dependences of normalized unit cell parameters $\frac{a}{a_0}$, $\frac{b}{b_0}$, $\frac{c}{c_0}$, $\frac{\beta}{\beta_0}$, $\frac{V}{V_0}$. *Circles* are data reported by Zhang et al. (1997). *Triangles* represent results of this study. *Error bars* are smaller than the symbol size

Table 5 Bulk modulus (K_{T0}) and its pressure derivatives (K'_{T0}) of hedenbergite

Composition	K_{T0} (GPa)	K'_{T0}	P_{max} (GPa)	Method	Reference
$Ca_{1.00}(Fe_{.67}Mn_{.16}Mg_{.17})Si_2O_6$, SC	131(4)	3.8(3)	29.91	X-ray	This study
$CaFeSi_2O_6$, SC	120	–	0	Brillouin	Kandelin and Weidner (1988)
$CaFeSi_2O_6$, PC	119(2)	4	3.7	X-ray	Zhang et al. (1990)
$CaFeSi_2O_6$, SC	117(1)	4.3(4)	10	X-ray	Zhang et al. (1997)

PC polycrystalline sample, *SC* single-crystal sample

and Downs 2000). The bulk modulus K_{T0} and K'_{T0} are determined to be 131(4) GPa and 3.8(3) in this study, as shown in Table 5. Considering the trade-off between K_{T0} and K'_{T0}, the confidence ellipses (with a confidence level of ±68.3 %) of this study and previous study are shown in Fig. 2. Previous study has a smaller bulk modulus K_{T0} and a wider range of K'_{T0}. Second-order Birch–Murnaghan equation of state (BM2) is also obtained with $K = 128.3(5)$ GPa.

Figure 3 shows the f_E–F_E plot, depicting a relationship between Eulerian strain f_E and Birch normalized stress F_E; thus, K_{T0} and K'_{T0} can also be determined from a weighted linear least-squares fitting (Hazen and Downs 2000).

$$F_E = K_{T0}\left[1 + 1.5f_E\left(K'_{T0} - 4\right)\right] \tag{4}$$

where

$$f_E = \left[(V/V_0)^{-2/3} - 1\right]\Big/2 \tag{5}$$

and

$$F_E = P\Big/\left[3f_E(1 + 2f_E)^{5/2}\right]. \tag{6}$$

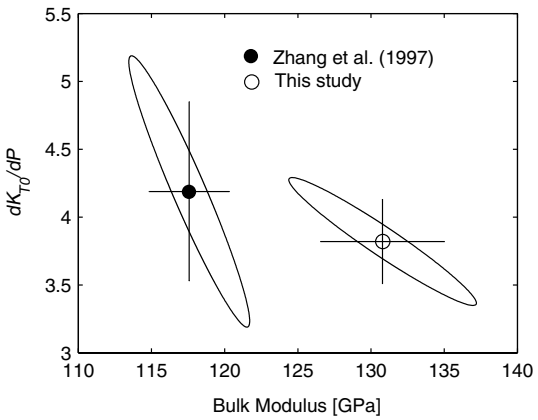

Fig. 2 Confidence ellipses in K_{T0} and K'_{T0} for the fit of the third-order Birch–Murnaghan equation of state to the hedenbergite *P*–*V* data. Data with the *filled circles* are from this study yielding $V_0 = 449.2(5)$ Å^3, $K_{T0} = 131(4)$ GPa and $K'_{T0} = 3.8(3)$. Data with the *open circles* represent Zhang et al.'s (1997) giving $V_0 = 449.8(1)$ Å^3, $K_{T0} = 118(3)$ GPa and $K'_{T0} = 4.2(7)$

In Eqs. (4)–(6), P is pressure and V and V_0 represent the volume at high and ambient pressures, respectively. $K_{T0} = 128(2)$ GPa and $K'_{T0} = 4.0(2)$ are determined using weighted linear least-squares fitting and are in good agreement with the results of BM3 fitting discussed above.

Polyhedral compression in hedenbergite

Figures 4, 5 and Table 6 report the bond lengths and polyhedron volumes of SiO_4 tetrahedron, FeO_6 octahedron and CaO_8 polyhedron. The three polyhedra show anisotropic compressibility, usually shorter bond lengths show lower compressibility and smaller polyhedra show lower compressibility. It is interesting to notice that there are crossovers in bond lengths for all three polyhedra; however, they do not seem to cause any discontinuous changes in the compression mechanism.

SiO_4 tetrahedron

SiO_4 tetrahedron has the smallest volume of ~2.1 Å^3 and shows the lowest volume compression of 2.0(1) × 10^{-3} GPa^{-1} between 1.9(1) GPa and 29.9(1) GPa, as shown in Table 6 and Fig. 5. Four unique pairs of bond lengths along with the average bond length are shown in Fig. 4a and Table 6. The average Si–O bond length decreases

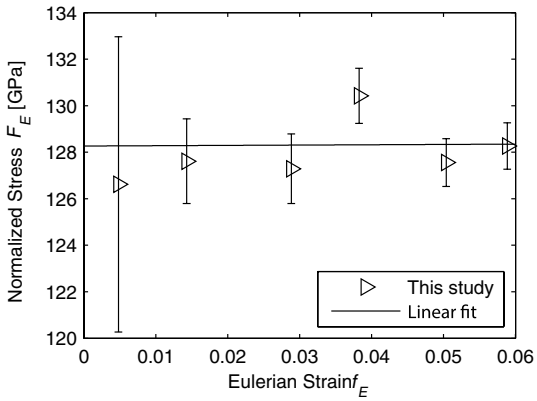

Fig. 3 Birch's normalized stress F_E versus the Eulerian strain f_E. *Triangles* represent the data from this study. Bulk modulus K and its pressure derivative calculated from linear fit of this study are $K_{T0} = 128(2)$ GPa and $K'_{T0} = 4.0(2)$

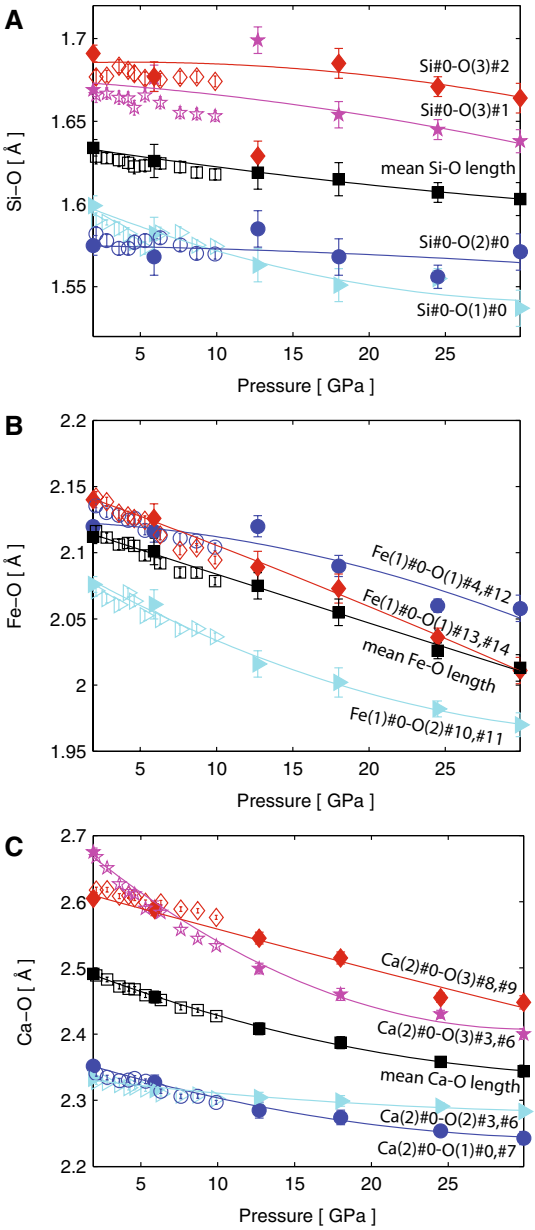

◀**Fig. 4** Bond lengths of hedenbergite. Data with *filled markers* are from this study, and those with *open markers* are from Zhang et al.'s (1997). **a** Si–O bond lengths of hedenbergite. There are four different Si–O bond lengths, Si#0–O(3)#2, Si#0–O(3)#1, Si#0–O(2)#0 and Si#0–O(1)#0, which are represented by *diamonds*, *pentagrams*, *right-pointing triangles* and *circles*, respectively. The average Si–O bond lengths are marked with *squares*. The 12.7(1) GPa data points were excluded when doing second-order polynomial fitting for Si#0–O(3)#2 and Si#0–O(3)#1. **b** Fe–O bond lengths of hedenbergite. Six bonds with three different bond lengths are reported here. Fe(1)#0–O(1)#14 and Fe(1)#0–O(1)#13 have the same length and are represented by *diamonds*. Fe(1)#0–O(2)#4 and Fe(1)#0–O(2)#12 have the same bond length and are represented by *circles*. *Triangle* markers stand for Fe(1)#0–O(2)#11 and Fe(1)#0–O(2)#10, while the average bond lengths are represented by *squares*. **c** Ca–O bond lengths are reported. Ca(2)#0–O(3)#6 and Ca(2)#0–O(3)#3 are represented by *pentagrams,* and Ca(2)#0–O(3)#9 and Ca(2)#0–O(3)#8 are marked with *diamonds*. Data with *circles* are Ca(2)#0–O(1)#0 and Ca(2)#0–O(1)#7, while those of Ca(2)#0–O(1)#3 and Ca(2)#0–O(1)#6 are marked with *triangles*. Average values are represented by *squares*

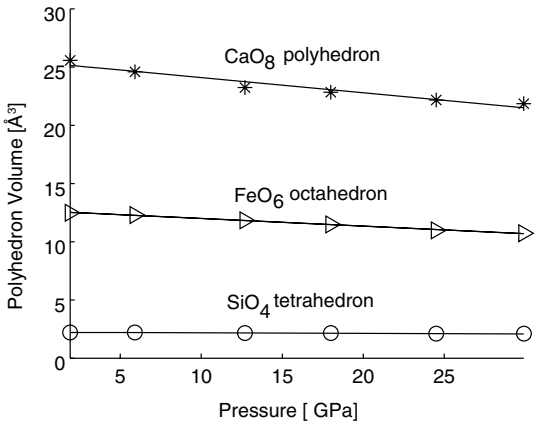

Fig. 5 Pressure dependences of SiO_4 (*circle*), FeO_6 (*triangle*) and CaO_8 (*asterisk*) polyhedral volumes in hedenbergite

continuously with a lowest compressibility of 1.07(8) $\times$ 10^{-3} GPa^{-1} among the three polyhedra, while individual bond behavior shows minor irregularities. Si#0–O(3)#2 is the longest bond between 0 GPa and 5.9(1) GPa, while Si#0–O(3)#1 is the second longest bond. These two bonds show anomalous behavior at 12.7(1) GPa; however, we attribute this anomaly to possible experimental error and omit that pressure point in polynomial fittings shown in Fig. 4a. A turnover is found in the two shorter Si–O bonds between 5.6(1) and 12.7(1) GPa.

M1 octahedron

Between 1.9(1) and 29.9(1) GPa, the volume of the M1 octahedron decreases from 12.48 to 10.72 $Å^3$ and shows a compressibility of 5.2(2) $\times$ 10^{-3} GPa^{-1}, as listed in Table 6 and Fig. 5. There are three different bond lengths in FeO_6 octahedron, and they show some anisotropy of compression behavior as shown in Fig. 4b and Table 6. The shortest bond Fe(1)#0–O(1)#11 shows a medium compression. Fe(1)#0–O(1)#14 is the longest bond at low pressure and shows the largest compressibility, while the second longest bond, Fe(1)#0–O(1)#4, displays the smallest compression among the three bonds, thus leading to a crossover of the two bonds somewhere between 5.9(1) and 12.7(1) GPa. This crossover was also observed by Zhang et al. (1997). The average bond displays a compressibility of 3.7(1) $\times$ 10^{-3} GPa^{-1} which is medium among the three polyhedra.

M2 polyhedron

As shown in Table 6 and Fig. 5, the larger polyhedral site, CaO_8, has a volume of 25.58 $Å^3$ at 1.9(1) GPa and

Table 6 Selected bond lengths (Å), angles (°), average bond length and polyhedral volume (Å^3) of hedenbergite up to 29.9(1) GPa

Pressure (GPa)	1.9(1)	5.9(1)	12.7(1)	18.0(1)	24.5(1)	29.9(1)
SiO_4 tetrahedron						
Si#0–O(1)#0	1.599(6)	1.58(1)	1.56(1)	1.55(1)	1.555(6)	1.54(1)
Si#0–O(2)#0	1.575(6)	1.57(1)	1.59(1)	1.57(1)	1.556(7)	1.57(1)
Si#0–O(3)#1	1.669(4)	1.676(8)	1.699(8)	1.654(8)	1.645(6)	1.638(7)
Si#0–O(3)#2	1.691(5)	1.677(9)	1.629(9)	1.685(9)	1.671(6)	1.664(9)
Mean Si–O length	1.634(5)	1.63(1)	1.62(1)	1.61(1)	1.607(6)	1.60(1)
O(1)#0–Si#0–O(3)#1	110.5(2)	110.9(4)	111.6(4)	111.9(5)	110.8(3)	110.5(5)
O(1)#0–Si#0–O(3)#2	110.4(3)	111.2(5)	112.6(5)	112.4(5)	113.1(3)	112.9(5)
O(2)#0–Si#0–O(1)#0	117.9(3)	117.1(5)	115.2(6)	115.2(6)	115.4(4)	115.1(6)
O(2)#0–Si#0–O(3)#1	109.9(3)	109.9(5)	110.0(4)	110.1(5)	111.3(3)	111.9(4)
O(2)#0–Si#0–O(3)#2	103.5(3)	103.8(4)	104.4(5)	104.8(5)	104.1(3)	104.5(5)
O(3)#1–Si#0–O(3)#2	103.5(2)	102.8(3)	102.1(3)	101.2(4)	101.0(2)	100.8(3)
Volume	2.2168	2.1857	2.1593	2.1423	2.1065	2.0910
σ^2	28.7800	27.8075	25.3124	27.8421	30.6758	29.9833
$\langle\lambda\rangle$	1.0070	1.0069	1.0068	1.0071	1.0078	1.0076
FeO_6 octahedron						
Fe(1)#0–O(2)#10	2.076(6)	2.06(1)	2.02(1)	2.00(1)	1.982(6)	1.970(9)
Fe(1)#0–O(2)#11	2.076(6)	2.06(1)	2.02(1)	2.00(1)	1.982(6)	1.970(9)
Fe(1)#0–O(1)#12	2.120(4)	2.116(8)	2.120(8)	2.090(8)	2.060(5)	2.06(1)
Fe(1)#0–O(1)#4	2.120(4)	2.116(8)	2.120(8)	2.090(8)	2.060(5)	2.06(1)
Fe(1)#0–O(1)#13	2.140(6)	2.13(1)	2.09(1)	2.07(1)	2.036(7)	2.01(1)
Fe(1)#0–O(1)#14	2.140(6)	2.13(1)	2.09(1)	2.07(1)	2.036(7)	2.01(1)
Mean Fe–O length	2.112(5)	2.10(1)	2.08(1)	2.06(1)	2.026(6)	2.01(1)
O(1)#12–Fe(1)#0–O(1)#13	92.2(2)	92.4(4)	92.3(4)	92.7(4)	93.1(3)	92.5(4)
O(1)#12–Fe(1)#0–O(1)#14	87.0(2)	88.1(4)	89.6(4)	89.1(4)	88.8(2)	88.8(4)
O(1)#13–Fe(1)#0–O(1)#14	80.7(3)	80.5(6)	80.8(6)	80.2(6)	81.8(4)	82.1(5)
O(1)#4–Fe(1)#0–O(1)#13	87.0(2)	88.1(4)	89.6(4)	89.1(4)	88.8(2)	88.8(4)
O(1)#4–Fe(1)#0–O(1)#14	92.2(2)	92.4(4)	92.3(4)	92.7(4)	93.1(3)	92.5(4)
O(2)#10–Fe(1)#0–O(1)#12	92.3(2)	91.7(3)	91.1(4)	91.0(3)	90.9(2)	90.9(3)
O(2)#10–Fe(1)#0–O(1)#14	93.6(2)	93.3(4)	91.5(4)	90.8(4)	88.2(3)	86.1(4)
O(2)#10–Fe(1)#0–O(1)#4	88.5(2)	87.9(4)	87.3(4)	87.4(4)	87.5(2)	88.1(4)
O(2)#10–Fe(1)#0–O(2)#11	92.4(3)	93.2(6)	96.3(6)	98.5(6)	102.0(4)	106.0(6)
O(2)#11–Fe(1)#0–O(1)#12	88.5(2)	87.9(4)	87.3(4)	87.4(4)	87.5(2)	88.1(4)
O(2)#11–Fe(1)#0–O(1)#13	93.6(2)	93.3(4)	91.5(4)	90.8(4)	88.2(3)	86.1(4)
O(2)#11–Fe(1)#0–O(1)#4	92.3(2)	91.7(3)	91.1(4)	91.0(3)	90.9(2)	90.9(3)
Volume	12.4836	12.2891	11.8387	11.4816	10.9788	10.7204
σ^2	14.6060	14.0974	14.3422	18.2916	23.1345	33.8212
$\langle\lambda\rangle$	1.0044	1.0042	1.0047	1.0057	1.0069	1.0100
CaO_8 polyhedron						
Ca(2)#0–O(1)#0	2.352(7)	2.33(1)	2.29(1)	2.27(1)	2.254(7)	2.24(1)
Ca(2)#0–O(1)#7	2.352(7)	2.33(1)	2.29(1)	2.27(1)	2.254(7)	2.24(1)
Ca(2)#0–O(2)#3	2.333(4)	2.316(7)	2.304(8)	2.299(8)	2.291(5)	2.283(9)
Ca(2)#0–O(2)#6	2.333(4)	2.316(7)	2.304(8)	2.299(8)	2.291(5)	2.283(9)
Ca(2)#0–O(3)#3	2.675(6)	2.592(9)	2.499(8)	2.460(9)	2.430(6)	2.400(8)
Ca(2)#0–O(3)#6	2.675(6)	2.592(9)	2.499(8)	2.460(9)	2.430(6)	2.400(8)
Ca(2)#0–O(3)#8	2.605(6)	2.588(9)	2.545(9)	2.515(9)	2.455(7)	2.45(1)
Ca(2)#0–O(3)#9	2.605(6)	2.588(9)	2.545(9)	2.515(9)	2.455(7)	2.45(1)
Mean Ca–O length	2.491(6)	2.456(9)	2.408(9)	2.387(9)	2.358(6)	2.344(9)
O(3)#8-Ca(2)#0–O(3)#3	59.98(9)	60.8(2)	61.8(2)	62.5(2)	63.2(1)	63.3(2)
O(3)#9-Ca(2)#0–O(3)#6	59.98(9)	60.8(2)	61.8(2)	62.5(2)	63.2(1)	63.3(2)

Table 6 continued

Pressure (GPa)	1.9(1)	5.9(1)	12.7(1)	18.0(1)	24.5(1)	29.9(1)
O(2)#3-Ca(2)#0–O(3)#8	62.3(2)	62.5(4)	63.0(3)	64.6(3)	64.8(2)	65.4(3)
O(2)#6-Ca(2)#0–O(3)#9	62.3(2)	62.5(4)	63.0(3)	64.6(3)	64.8(2)	65.4(3)
O(3)#8-Ca(2)#0–O(3)#6	67.1(2)	67.0(3)	66.8(3)	67.1(3)	68.1(2)	69.1(3)
O(3)#9-Ca(2)#0–O(3)#3	67.1(2)	67.0(3)	66.8(3)	67.1(3)	68.1(2)	69.1(3)
O(1)#0-Ca(2)#0–O(1)#7	72.2(3)	72.4(5)	72.7(6)	71.9(5)	72.5(3)	72.1(5)
O(2)#3-Ca(2)#0–O(1)#7	80.5(2)	80.4(3)	80.1(3)	79.4(3)	78.7(2)	78.8(4)
O(2)#6-Ca(2)#0–O(1)#0	80.5(2)	80.4(3)	80.1(3)	79.4(3)	78.7(2)	78.8(4)
O(2)#3-Ca(2)#0–O(1)#0	81.9(2)	80.6(3)	78.1(3)	77.2(3)	76.2(2)	74.3(4)
O(2)#6-Ca(2) #0–O(1)#7	81.9(2)	80.6(3)	78.1(3)	77.2(3)	76.2(2)	74.3(4)
O(3)#8-Ca(2)#0–O(3)#9	82.5(2)	83.1(4)	84.7(4)	83.1(4)	84.8(3)	85.4(4)
O(2)#3-Ca(2)#0–O(3)#6	85.2(2)	86.3(3)	88.4(3)	88.3(3)	89.3(2)	91.1(3)
O(2)#6-Ca(2)#0–O(3)#3	85.2(2)	86.3(3)	88.4(3)	88.3(3)	89.3(2)	91.1(3)
O(1)#7-Ca(2)#0–O(3)#6	90.9(2)	90.6(3)	90.4(3)	89.6(3)	88.5(2)	88.0(3)
O(1)#0-Ca(2)#0–O(3)#3	90.9(2)	90.6(3)	90.4(3)	89.6(3)	88.5(2)	88.0(3)
Volume	25.5778	24.5878	23.2452	22.8337	22.1611	21.8551
σ^2	149.5173	147.1162	148.4800	132.6054	129.4928	133.7569
$\langle\lambda\rangle$	0.9567	0.9537	0.9515	0.9462	0.9393	0.9350
O3–O3–O3	163.7(2)	161.9(4)	161.7(4)	158.4(4)	159.4(3)	158.1(4)

Symmetry transformations used to generate equivalent atoms are given below: #0 x, y, z; #1 x, y, z−1; #2 x, $-y$, $z-1/2$; #3 $-x+1/2$, $-y+1/2$, $-z+1$; #4 $-x$, $-y+1$, $-z$; #5 $x+1/2$, $y-1/2$, z; #6 $x-1/2$, $-y+1/2$, $z-1/2$; #7 $-x$, y, $-z+1/2$; #8 $-x+1/2$, $y+1/2$, $-z+3/2$; #9 $x-1/2$, $y+1/2$, $z-1$; #10 $x-1/2$, $y+1/2$, z; #11 $-x+1/2$, $y+1/2$, $-z+1/2$; #12 x, $-y+1$, $z+1/2$; #13 x, $y+1$, z; #14 $-x$, $y+1$, $-z+1/2$; #15 $-x$, $-y+2$, $-z+1$; #16 $-x$, $-y+2$, $-z$; #17 $-x$, $-y+1$, $-z+1$; #18 x, $y-1$, z; #19 x, y, $z+1$; #20 x, $-y$, $z+1/2$; #21 $x+1/2$, $y-1/2$, $z+1$

21.96 Å^3 at 29.9(1) GPa and is characterized by an average compressibility of 5.1(7) × 10^{-3} GPa^{-1} from 1.9(1) to 29.9(1) GPa. Four unique bond lengths are shown in Fig. 4c and Table 6. The longest bond Ca(2)#0–O(3)#6 shows the highest compressibility, while the second longest bond Ca(2)#0–O(3)#9 displays a second largest compressibility; therefore, a crossover is observed at ~5.9(1) GPa. The shortest bond is Ca(2)#0–O(2)#6 and shows a smallest compression, while the second shortest bond Ca(2)#0–O(2)#3 has a second smallest compression, with a turnover of these two bond lengths at ~5.5(1) GPa. The average bond length reveals a compressibility of 5.2(6) × 10^{-3} GPa^{-1} which is the highest among the three polyhedra.

Raman spectroscopy

Raman spectroscopy experiments were conducted on the same hedenbergite sample up to ~33 GPa. The Raman spectra of hedenbergite at 2.0(1), 17.4(1) and 32.8(1) GPa are shown in Fig. 6a. The peaks are fit with a Gaussian function and labeled ν_1–ν_{13} (Fig. 6b). Our results show a good agreement with previous ambient study (Table 7) by Huang et al. (2000) and the data from University of Arizona RRUFF collection database. In our experiment, 13 Raman modes were observed between 200 and 1200 cm^{-1}. Group theory analysis predicts 20 Raman active modes (Rutstein and White 1971). The reason why there are less observed modes in our experiments may be that some modes are too weak to be detected by our spectrometer or the spatial resolution is not sufficient to distinguish peaks that are very close to each other. Due to cation substitution in the M1 site, broadening of the M–O bend/stretch modes are expected (Gatta et al. 2005; Huang et al. 2000).

Discussion

Compression mechanism

Hedenbergite belongs to chain silicates, with single chains of SiO_4 tetrahedron along the c axis, sandwiched by FeO_6 octahedron and CaO_8 polyhedron sheets, oriented in b–c plane. The SiO_4 tetrahedron, FeO_6 octahedron and CaO_8 polyhedron constitute about 38 % volume of the unit cell. These polyhedra are compressed by ~15 % between 1.7(1) and 29.9(1) GPa.

In this study, the axial compressibilities of a, b and c are calculated to be 1.7(2), 4.9(5), 2.13(9) × 10^{-3} GPa^{-1}. Zhang et al. (1997) adopted a different compressibility fitting algorithm, which causes an apparent discrepancy in values. Recalculating the axial compressibility of Zhang et al.'s (1997) with our method yields 2.3(9), 4(1) and

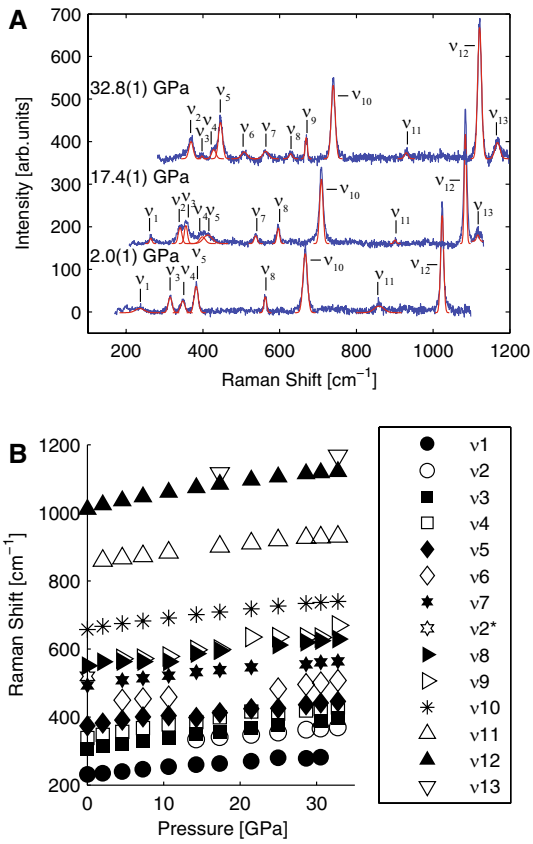

Fig. 6 **a** Raman spectra of hedenbergite at 2.0(1), 17.4(1) and 32.8(1) GPa. **b** Raman peak positions of hedenbergite up to ~33 GPa

$2.9(5) \times 10^{-3}$ GPa^{-1} for *a*, *b* and *c* axis, respectively. Our results show similar pattern in the ratio of 1:2.83:1.22, as compared to 1:1.77:1.28 determined by the previous authors. In general, *b* shows the highest compressibility and *c* axis is more compressible than *a*. Brillouin scattering determined the elastic moduli C_{11}, C_{22} and C_{33} to be 222(6), 176(5) and 249(5) GPa (Kandelin and Weidner 1988), which correlates well with our axial compressibility ratios. However, our results show that *b* axis is more compressible than indicated by the previous data. Diopside is a Ca, Mg end-member pyroxene, which is related to hedenbergite by substituting Fe^{2+} with Mg^{2+}. We calculated the compressibility of diopside (Zhang et al. 1997) with our method and obtained 3(1), 4(1) and $3.0(5) \times 10^{-3}$ GPa^{-1} for *a*, *b* and *c* axes. Similar to hedenbergite, also in diopside, the *b* axis has the highest compressibility. However, in contrast to hedenbergite, where *c* axis is more compressible than *a*, *a* and *c* have almost equal axial compressibility in diopside. The decrease in compressibility of *c* axis in diopside may be caused by the lower compressibility of MgO_6 compared to FeO_6 along the chain (Zhang et al. 1997). Different pressure range of data can also contribute to the discrepancy between our data and Zhang et al.'s (1997).

Figure 2 presents the confidence ellipses of this study and Zhang et al.'s (1997) data calculated by our method. We obtained $K_{T0} = 131(4)$ GPa and $K'_{T0} = 3.8(3)$ for this study and $K_{T0} = 118(3)$ GPa and $K'_{T0} = 4.2(7)$ for Zhang et al.'s (1997). Our results show higher bulk modulus K_{T0} but lower K'_{T0}. The discrepancy between these two data is likely due to the trade-off between K_{T0} and K'_{T0}, but could also be related to the compositional differences and different pressure ranges. For the diopside data (Zhang et al. 1997), the bulk modulus and its pressure derivative calculated with our method are $K_{T0} = 108.3(3)$ GPa and $K'_{T0} = 5.4(6)$. Comparing hedenbergite and diopside, the latter has lower bulk modulus, which was also noted by Zhang et al. (1997).

The geometry of the SiO_4 tetrahedral chain and pressure evolution of the O3–O3–O3 angle are shown in Fig. 7 and Table 6. The angle O3–O3–O3 (θ in Fig. 7a) is defined by the O3 atoms which form the two longest bonds with Si as shown by the red and magenta bonds in Fig. 7b, c (color of the bonds is consistent with Fig. 4a). The O3–O3–O3 angle is 163.7(2)° at 1.9(1) GPa and decreases, in general, as pressure increases which contributes to the axial compression along with the bond length decrease. The O3–O3–O3 angle remains almost unchanged from 5.9(1) to 12.7(1) GPa and even increases from 18.0(1) to 24.5(1) GPa; therefore, the decrease in Si–O3 bond lengths contributes mostly to the *c* axis compression in these pressure ranges.

Polyhedral distortion in hedenbergite

The polyhedral distortion can be described by angle variance and mean quadratic elongation parameters proposed by Robinson et al. (1971). The angle variance of the three polyhedra is shown in Fig. 8a. Angle variance is defined as $\sigma^2 = \sum_{i=1}^{n} \left[(\theta_i - \theta_0)^2/(n-1)\right]$, where θ_i is the *i*th angle, θ_0 is the angle of ideal polyhedron of the same volume and *n* is the number of bonds. SiO_4 tetrahedron shows a medium angle variance of ~30 and remains almost constant as pressure changes. FeO_6 octahedron shows the smallest angle variance of ~14 at low pressure and starts to increase somewhere between 12.7(1) and 18.0(1) GPa and reaches ~33 at 29.9(1) GPa. The CaO_8 polyhedron is already quite distorted at ambient conditions and has the largest angle variance of ~150; however, the distortion decreases linearly with pressure. It is interesting to notice that the drop in angle variance somewhere between 18.0(1) to 24.5(1) GPa can be the main factor that contributes to the decrease in CaO_8 polyhedral compressibility starting from 18.0(1) GPa.

Table 7 Assignment and frequencies (cm^{-1}) of observed Raman modes up to 32.8(1) GPa with comparison of reference

Assignment	Huang et al. (2000)	0.0(1)[a] GPa	2.0(1) GPa	4.6(1) GPa	7.3(1) GPa	10.7(1) GPa	14.3(1) GPa	17.4(1) GPa	21.5(1) GPa	25.0(1) GPa	28.6(1) GPa	30.6(1) GPa	32.8(1) GPa	Mode
M–O stretch/bend	234	231.5	235.3	240.3	247.1	254.1	259.6	264.2	269.8	279.6	278.4	281.5	–	1
	242	–	–	–	–	–	–	–	–	–	–	–	–	1*
	–	–	–	–	–	–	334.6	340.5	347.9	354.7	363.5	365.9	369.0	2
	304	304.8	314.6	322.0	329.8	338.4	348.6	355.6	368.3	375.4	–	388.2	397.3	3
	333	338.6	347.5	356.6	367.4	378.3	384.8	398.8	416.2	409.9	419.0	424.3	428.3	4
	372	373.9	382.4	391.1	400.2	403.8	398.5	412.7	–	425.6	435.9	441.0	445.8	5
	–	–	–	449.3	453.3	458.7	–	–	–	–	–	–	507.6	6
O–Si–O bend	492	492.7	–	508.1	514.0	521.2	531.9	537.5	545.7	–	–	560.2	563.6	7
	521	519.7	–	–	–	–	–	–	–	–	–	–	–	2*
	547	550.6	562.5	562.6	562.6	562.1	586.2	596.4	–	611.4	619.6	624.1	628.8	8
	–	–	–	–	571.6	578.1	597.2	–	634.9	634.5	634.2	633.9	669.2	9
Si–O stretch	659	657.1	666.6	674.5	682.4	691.0	701.1	708.7	717.7	725.9	733.8	736.6	739.7	10
	855	–	859.1	866.5	872.6	883.1	–	901.0	910.0	919.3	926.5	927.7	930.1	11
	1012	1010.5	1023.6	1035.2	1047.3	1060.4	1074.2	1084.1	1096.1	1105.8	1115.0	1117.9	1121.2	12
	1027	–	–	–	–	–	–	1115.9	–	1145.6	–	–	1167.8	13

Modes with * are not observed by this study. [a] The ambient pressure point data are from the University of Arizona RRUFF collection #R070236

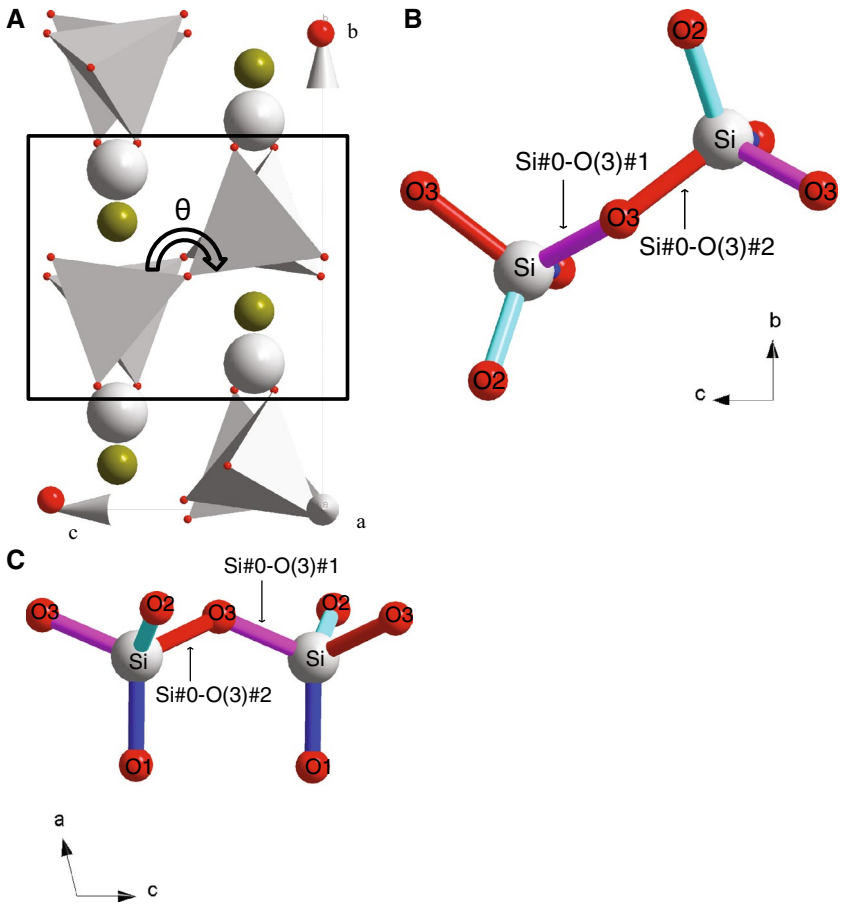

Fig. 7 **a** Polyhedral illustrations of the SiO_4 tetrahedral chain, θ is O3–O3–O3 angle. **b** Illustration of bonds in SiO_4 tetrahedron viewed along *a* axis. **c** Illustration of bonds in SiO_4 tetrahedron viewed along *b* axis. *Colors* of the bonds are consistent with Fig. 4a

Mean quadratic elongation is defined as $\langle\lambda\rangle = \sum_{i=1}^{n}\left[(l_i/l_0)^2/n\right]$, where l_0 is the center-to-vertex distance of a regular polyhedron of the same volume, l_i is the ith center-to-vertex distance and n is the number of bonds. In Fig. 8b, both SiO_4 and FeO_6 show a mean quadratic elongation >1. The mean quadratic elongation of SiO_4 remains almost constant as pressure changes, just like in the case of the angle variance. However, the quadratic elongation of FeO_6 starts to increase somewhere between 12.7(1) and 18.0(1) GPa, which indicates an increase in distortion. CaO_8 has a mean quadratic elongation <1, which decreases gradually as pressure increases, also indicating increasing distortion.

Raman mode variation with pressure

Modes are assigned by comparing our results with previous ambient pressure data (Huang et al. 2000). Four modes (ν_1–ν_6) are assigned to M–O stretch or O–M–O bend (M = Ca^{2+}, Fe^{2+}, Mg^{2+}, Mn^{2+}), three modes (ν_7–ν_9) are assigned to O–Si–O bend, and four modes (ν_{10}–ν_{13}) are assigned to Si–O stretch. Two additional modes (ν_1*, ν_2*) are reported by Huang et al. (2000), but not in this study. The reason for this may be that these peaks are too weak or the difference in chemical composition and ordering causes them to be obscured. Our study also observed three modes ν_2, ν_6 and ν_9 that were not reported previously. These peaks are very weak at low pressure and as pressure increases, they start to diverge, as shown in Fig. 6. Such phenomenon was also observed by Gatta et al. (2005). The reason for the divergence of the two peaks may be the anisotropic compression making the crystal distorted, thus enhancing the difference between two peaks. In general, frequency increases as pressure increases, since compression generally strengthens bond, thus increasing the force constants. It is interesting to notice some discontinuities as frequencies increase. These phenomena are related to the discontinuous change in bond length and angles in the structure.

Conclusions

We reported results of high-pressure single-crystal X-ray diffraction and Raman spectroscopy experiments conducted on natural Ca, Fe end-member pyroxene (hedenbergite) up to ~33 GPa in diamond anvil cell. Unit cell parameters exhibit continuous decrease on compression. Axial compressibilities of hedenbergite up to ~30 GPa are

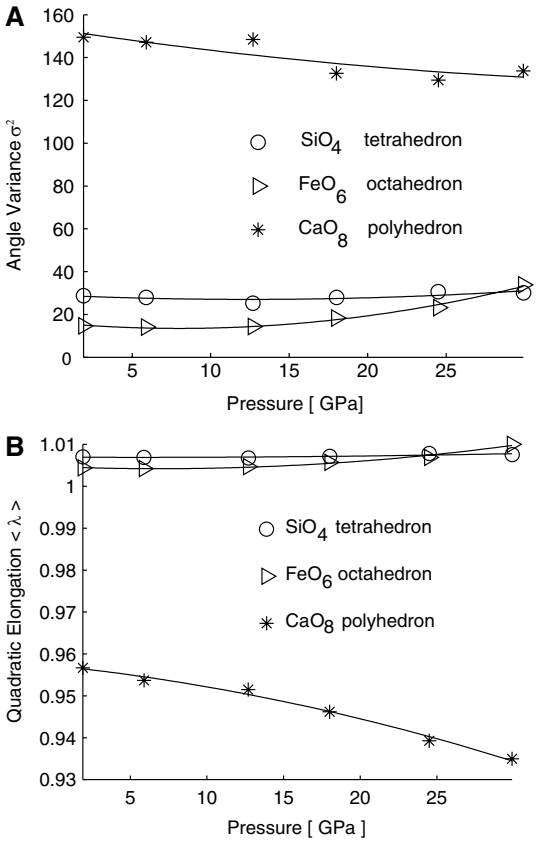

Fig. 8 Angle variance (**a**) and quadratic elongation (**b**) of SiO_4 (*circle*), FeO_6 (*triangle*) and CaO_8 (*asterisk*) in hedenbergite up to 29.9(1) GPa

calculated to be 1.7(2), 4.9(5) and 2.13(9) $\times$ 10^{-3} GPa^{-1}, respectively, and show a highest compressibility of *b* and lowest compressibility of *a*. Our data show similar results in compressibilities with previous studies. Diopside shows a highest compressibility of *b* but almost equal compressibilities of *a* and *c*. The difference between hedenbergite and diopside may be caused by the different compressibilities of FeO_6 and MgO_6 polyhedra. Bulk modulus and its pressure derivate for hedenbergite are calculated to be 131(4) GPa and 3.8(3), respectively, by fitting third-order Birch–Murnaghan equation of state. The bulk modulus of hedenbergite is higher than that of diopside (108.3(3) GPa), but its pressure derivative is lower than that of diopside (5.4(6)).

Bond lengths are also discussed in this study. Generally, longer bonds show higher compressibilities except for some of the Si–O bonds. SiO_4, the smallest polyhedron, shows the lowest compressibility. Angle and elongation distortions are observed in three polyhedra at high pressure. Thirteen vibrational modes are observed with Raman spectroscopy up to ~33 GPa. In general, mode frequencies increase as pressure increase.

Acknowledgments The project was supported by the National Science Foundation Division of Earth Sciences Geophysics Grant No. 1344942. Portions of this work were performed at GeoSoilEnviroCARS (Sector 13), Advanced Photon Source (APS), and Argonne National Laboratory. GeoSoilEnviroCARS is supported by the National Science Foundation—Earth Sciences (EAR-1128799) and Department of Energy—Geosciences (DE-FG02-94ER14466). Use of the Advanced Photon Source was supported by the US Department of Energy, Office of Science, Office of Basic Energy Sciences, under Contract No. DE-AC02-06CH11357. We would also like to thank Carnegie-DOE Alliance Center for support through Academic Partner subcontract to PD and Prof. R. T. Downs at the University of Arizona for kindly providing the samples from RRUFF collections. We would like to thank the two reviewers, Diego Gatta and Jennifer Kung for helpful comments.

References

Bina CR (2013) Mineralogy: garnet goes hungry. Nat Geosci 6(5):335–336

Cameron M, Papike JJ (1981) Structural and chemical variations in pyroxenes. Am Miner 66(1–2):1–50

Cameron M, Sueno S, Prewitt C, Papike J (1973) High-temperature crystal chemistry of acmite, diopside, hedenbergite, jadeite, spodumene, and ureyite. Am Miner 58:594–618

Chermak JA, Rimstidt JD (1989) Estimating the thermodynamic properties (Delta G of and Delta H of) of silicate minerals at 298 K from the sum of polyhedral contributions. Am Miner 74(9–10):1023–1031

Dera P, Finkelstein GJ, Duffy TS, Downs RT, Meng Y, Prakapenka V, Tkachev S (2013a) Metastable high-pressure transformations of orthoferrosilite Fs82. Phys Earth Planet Inter 221:15–21

Dera P, Zhuravlev K, Prakapenka V, Rivers ML, Finkelstein GJ, Grubor-Urosevic O, Tschauner O, Clark SM, Downs RT (2013b) High pressure single-crystal micro X-ray diffraction analysis with GSE_ADA/RSV software. High Press Res 33:466–484

Finkelstein GJ, Dera PK, Duffy TS (2014) Phase transitions in orthopyroxene (En_{90}) to 49 GPa from single-crystal X-ray diffraction. Phys Earth Planet Inter (in press)

Gatta GD, Ballaran TB, Iezzi G (2005) High-pressure X-ray and Raman study of a ferrian magnesian spodumene. Phys Chem Miner 32(2):132–139

Hazen RM, Downs RT (2000) High-temperature and high-pressure crystal chemistry. Mineralogical Society of America, Blacksburg

Huang E, Chen CH, Huang T, Lin EH, Xu JA (2000) Raman spectroscopic characteristics of Mg–Fe–Ca pyroxenes. Am Miner 85(3–4):473–479

Ita J, Stixrude L (1992) Petrology, elasticity, and composition of the mantle transition zone. J Geophys Res 97(B5):6849–6866

Jiang G, Zhao D, Zhang G (2008) Seismic evidence for a metastable olivine wedge in the subducting Pacific slab under Japan Sea. Earth Planet Sci Lett 270(3):300–307

Jiang G, Zhao D, Zhang G (2015) Detection of metastable olivine wedge in the western Pacific slab and its geodynamic implications. Phys Earth Planet Inter 238:1–7

Kandelin J, Weidner DJ (1988) Elastic properties of hedenbergite. J Geophys Res (1978–2012) 93(B2):1063–1072

Kaneshima S, Okamoto T, Takenaka H (2007) Evidence for a metastable olivine wedge inside the subducted Mariana slab. Earth Planet Sci Lett 258(1):219–227

Kim Y-H, Ming LC, Manghnani MH (1989) A study of phase transformation in hedenbergite to 40 GPa at ~1200 °C. Phys Chem Miner 16(8):757–762

Kim Y-H, Ming L, Manghnani M, Ko J (1991) Phase transformation studies on a synthetic hedenbergite up to 26 GPa at 1200 °C. Phys Chem Miner 17(6):540–544

Krot AN, Brearley AJ, Petaev MI, Kallemeyn GW, Sears DW, Benoit PH, Hutcheon ID, Zolensky ME, Keil K (2000) Evidence for low-temperature growth of fayalite and hedenbergite in MacAlpine Hills 88107, an ungrouped carbonaceous chondrite related to the CM–CO clan. Meteorit Planet Sci 35(6):1365–1386

Mao HK, Xu J, Bell PM (1986) Calibration of the ruby pressure gauge to 800 kbar under quasi-hydrostatic conditions. J Geophys Res 91:4673–4676

Meinert LD (1992) Skarns and skarn deposits. Geosci Canada 19(4):145–162

Nishi M, Kato T, Kubo T, Kikegawa T (2008) Survival of pyropic garnet in subducting plates. Phys Earth Planet Inter 170(3–4):274–280

Nishi M, Kubo T, Ohfuji H, Kato T, Nishihara Y, Irifune T (2013) Slow Si–Al interdiffusion in garnet and stagnation of subducting slabs. Earth Planet Sci Lett 361:44–49

Plonka AM, Dera P, Irmen P, Rivers ML, Ehm L, Parise JB (2012) β-Diopside, a new ultrahigh-pressure polymorph of $CaMgSi_2O_6$with six-coordinated silicon. Geophys Res Lett 39(24):L24307

Ringwood AE (1967) The pyroxene-garnet transformation in the earth's mantle. Earth Planet Sci Lett 2(3):255–263

Ringwood AE (1975) Composition and petrology of the earth's mantle. McGraw-Hill Inc.

Ringwood AE (1982) Phase transformations and differentiation in subducted lithosphere: implications for mantle dynamics, basalt petrogenesis, and crustal evolution. J Geol 90(6):611–643

Rivers ML, Prakapenka VB, Kubo A, Pullins C, Hall CM, Jacobsen SD (2008) The COMPRES/GSECARS gas loading system for diamond anvil cells at the Advanced Photon Source. High Press Res 28:273–292

Robinson K, Gibbs GV, Ribbe PH (1971) Quadratic elongation: a quantitative measure of distortion in coordination polyhedra. Science 172(3983):567–570

Rutstein M, White W (1971) Vibrational spectra of high-calcium pyroxenes and pyroxenoids. Am Miner 56(5–6):877

Sheldrick GM (2008) A short history of SHELX. Acta Cryst A64:112–122

Van Hinsberg V, Vriend S, Schumacher J (2005a) A new method to calculate end-member thermodynamic properties of minerals from their constituent polyhedra I: enthalpy, entropy and molar volume. J Metamorph Geol 23(3):165–179

Van Hinsberg V, Vriend S, Schumacher J (2005b) A new method to calculate end-member thermodynamic properties of minerals from their constituent polyhedra II: heat capacity, compressibility and thermal expansion. J Metamorph Geol 23(8):681–693

Van Mierlo W, Langenhorst F, Frost D, Rubie D (2013) Stagnation of subducting slabs in the transition zone due to slow diffusion in majoritic garnet. Nat Geosci 6(5):400–403

Wood BJ, Blundy JD (1997) A predictive model for rare earth element partitioning between clinopyroxene and anhydrous silicate melt. Contrib Miner Petrol 129(2–3):166–181

Zhang L, Ahsbahs H, Turk P-G, Hafner SS (1990) A pressure induced phase transition in pyroxene. High Press Sci Technol 5(1-6):732–734

Zhang L, Ahsbahs H, Hafner SS, Kutoglu A (1997) Single-crystal compression and crystal structure of clinopyroxene up to 10 GPa. Am Miner 82:245–258

Zhang L, Stanek J, Hafner SS, Ashbahs H, Grunsteudel HF, Metge J, Ruffer R (1999) ^{57}Fe nuclear forward scattering of synchrotron radiation in hedenbergite CaFeSi2O6 at hydrostatic pressures up to 68 GPa. Am Miner 84:447–453

Zhang JS, Dera P, Bass JD (2012) A new high-pressure phase transition in natural Fe-bearing orthoenstatite. Am Miner 97(7):1070–1074